Improving Brightness Temperature Measurements near Coastal Areas for SMAP

Julian Chaubell, Simon Yueh, Jinzheng Peng, Scott Dunbar, Steven Chan, Fan Chen, Jeffrey Piepmeier, Rajat Bindlish, Dara Entekhabi, Peggy O'Neill

***Abstract*— The Soil Moisture Active Passive (SMAP) mission is designed to acquire L-band radiometer measurements for the estimation of soil moisture with 0.04 m^3/m^3 volumetric accuracy in the top 5 cm for vegetation with water content of less than 5 kg/m^2. In regions near the coast or near inland bodies of water, the signal measured by the SMAP radiometer contains emissions from land and water, resulting in errors in the soil moisture estimation. In this paper, the effort to extract the brightness temperature (TB) according to the land fraction or water fraction (depending on the center of the footprint location) from the affected SMAP measurements was addressed. A single pixel correction algorithm was applied and its performance was evaluated over simulated data. A data-driven approach for the estimation of land and water TB for data correction was developed. The correction algorithm was then applied to real data and its performance was assessed over the SMAP soil moisture retrievals. We showed that the single pixel algorithm is an effective and computationally efficient algorithm for removing land or water TB contamination from the SMAP data.**

***Index Terms*—Brightness Temperature, Coastal areas, Land contamination, SMAP, Water contamination.**

I. Introduction

The Soil Moisture Active Passive (SMAP) mission was launched on Jan 31, 2015 [1]. The mission is designed to acquire and combine L-band radar and radiometer measurements for the estimation of soil moisture with 0.04 m^3/m^3 volumetric accuracy (1-sigma). The radar operated until July 7, 2015. Since then, the focus of SMAP project is to improve radiometer-only based soil moisture algorithm. In regions near the coast or near inland bodies of water, the signal measured by the SMAP radiometer contain emissions from land and water, resulting in errors in the soil moisture estimation. The mixed land and water emissions lead to an underestimation of land brightness temperature (TB), leading to an overestimation of soil moisture. Fig. 1 displays a view of the Great Lakes. Fig. 1 (a) shows the TB map featuring the smooth transition of the water/land interface due to land/water contamination (cyan bands). Fig. 1 (b) shows the corresponding soil moisture map. The bright cyan and blue rings (wet soil) around the lakes are the result of water contamination on the brightness temperatures (TBs) over land.

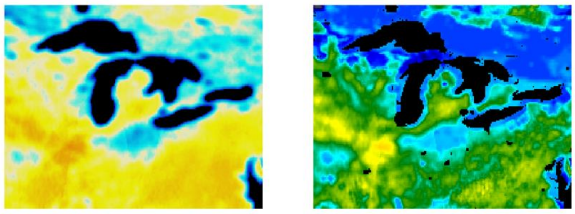

(a) (b)

Fig. 1. (a) SMAP TB map of the Great Lakes showing cyan bands at the edges of the lakes caused by the land/water contamination. (b) Corresponding soil moisture map with presence of cyan and blue bands around the lakes indicating an overestimation of soil moisture.

The removal of water emissions contributing to the sensor measurement will reduce the soil moisture bias near coastal zones, and will also improve the retrieval of other physical parameters. Several articles have addressed the separation of the mixed land and water TBs using different techniques to improve, for example, Special Sensor Microwave Imager (SSM/I) products. Bennartz [2] introduced a single pixel algorithm (SPA) to correct the coastal SSM/I measurements and then used the corrected TBs to retrieve columnar water vapor content. This technique requires that the fraction of land in the radiometer footprint and the land TBs in the nearby areas are known. A similar technique is used in [3] to correct the coastal TB and then retrieves sea ice concentration near coastal areas in the Baltic Sea. Bellerby [4] used a technique that retrieves the land and sea TB with multi-pixel information (MPA); once the TBs were corrected, the data were used for wind retrievals over the Great Lakes. This technique assumes

The work described in this paper was carried out by the Jet Propulsion Laboratory, California Institute of Technology under a contract with the National Aeronautics and Space Administration.

Julian Chaubell, Steven Chan, Scott Dunbar and Simon Yueh, are with the Jet Propulsion Laboratory, California Institute of Technology, Pasadena, CA 91109 USA. (email: julian@jpl.nasa.gov; Steventsz.K.Chan@jpl.nasa.gov; Roy.S.Dunbar@jpl.nasa.gov; simon.yueh@jpl.nasa.gov)

Rajat Bindlish, Peggy O'Neill, Jinzheng Peng and Jeffrey Piepmeier are with the Goddard Space Center, Greenbelt, MD, USA. (email: rajat.bindlish@nasa.gov; peggy.e.oneill@nasa.gov; jinzheng.peng@nasa.gov; jeffrey.r.piepmeier@nasa.gov).

Fan Chen is with USDA Agricultural Research Service, Beltsville, MD, USA (email: fan.chen@ars.usda.gov)

Dara Entekhabi is with the Massachusetts Institute of Technology, Cambridge, Massachusetts, USA (email: darae@mit.edu).

that the TB is constant within the area covered by the used set of measurements, thus reducing the product resolution [5]. In addition, the MPA for SMAP would increase significantly the latency of SMAP TB product, and consequently will especially affect the near-real time soil moisture products. For those reasons, the MPA is not considered for the SMAP data correction. Yang [5] and Desportes [6] compared different techniques and analyzed the sources of error for those techniques. In [6] the authors found that, among the techniques they studied, the approach used in [2] presented the best performance when applied to the Topography Experiment (TOPEX) Microwave Radiometer for the correction of wet path delay measurements.

In this work, the SPA approach was applied to separate the land and water contribution for the uncorrected SMAP measurements. SPA approach removes the bias over the coastal areas without significantly compromising the latency of the product. Preliminary work was presented in [7]. The methodology for the correction of land and water TBs is summarized in Section II. The results using simulated data are presented in Section III. The results using SMAP observations are shown in Section IV. The validation of our approach is given in Section V and a summary in Section VI.

II. Correction Methodology for Water and Land Brightness Temperature

The single pixel technique we applied for the separation of land and water TB requires that the fractions of land and water in the radiometer field of view are known. The major error sources in this correction approach are uncertainties in the estimated TB (land or water) and uncertainties in the land fraction, arising from errors in the antenna pattern, land mask, or instrument geolocation as well as pointing errors [2]. The land and water fractions were estimated using the measured SMAP antenna patterns along with a static land mask defined over a 1 km Equal-Area Scalable Earth Grid 2.0 (EASE2). Note that the use of a static land mask is a limitation for capturing seasonal changes in inland water bodies.

The brightness temperature T_B measured by the radiometer is modeled by the convolution of the antenna gain pattern with the actual distribution of brightness temperature T_b over the surface of the earth:

$$T_B(\hat{s}_0) = \frac{\int G(\hat{s}_0, \hat{s}) T_b(\hat{s}) d\Omega}{\int G(\hat{s}_0, \hat{s}) d\Omega}, \quad (1)$$

where $\hat{s}_0$ is the center of the footprint projection, and $G(\hat{s}_0, \hat{s})$ is the antenna gain pattern center at $\hat{s}_0$ and evaluated over the surface point $\hat{s}$. Equation (1) can be separated into the land and water contribution as follows:

$$T_B(\hat{s}_0) = \frac{1}{\int G(\hat{s}_0, \hat{s}) d\Omega} \left(\begin{array}{l} \int G(\hat{s}_0, \hat{s}) \big(1 - M(\hat{s})\big) T_b(\hat{s}) d\Omega \\ + \int G(\hat{s}_0, \hat{s}) M(\hat{s}) T_b(\hat{s}) d\Omega \end{array} \right), \quad (2)$$

where $M(x)$ is the land mask defined over a 1 km EASE2 grid. $M(x) = 1$ if x is over water and $M(x) = 0$ if x is over land. Assuming that $T_b = T_B^{land}$ is constant over the land portion of the domain of integration and that $T_b = T_B^{water}$ is constant over the water portion of the domain of integration, then we have

$$T_B(\hat{s}_0) = (1 - f) T_B^{land} + f T_B^{water}, \quad (3)$$

where f is the water fraction given by

$$f = \frac{\int G(\hat{s}_0, \hat{s}) M(\hat{s}) d\Omega}{\int G(\hat{s}_0, \hat{s}) d\Omega}, \quad (4)$$

While the standard and enhanced SMAP products follow the same correction algorithm, the implementation over the enhanced product requires a modification in the computation of the water fraction. The enhanced SMAP product provides an optimal interpolation of the radiometer measurements onto a global 9 km EASE2 using Backus-Gilbert (BG) interpolation [8], [9]. The objective of the BG interpolation as implemented by SMAP is to achieve optimal TB estimates at the center of the grid cells as if original observations were available at the same locations [9]. Following the deduction in [9], we computed the water fraction using the BG interpolation,

$$f = \sum_{i=1}^{N} a_i f_i \quad (5)$$

where a_i are the same Backus-Gilbert coefficients used for the interpolation of the antenna temperature and f_i is the water fraction corresponding to the SMAP measurements used for the Backus-Gilbert interpolation given by

$$f_i = \frac{\int G\big(\hat{s}_0^i, \hat{s}\big) M(\hat{s}) d\Omega}{\int G\big(\hat{s}_0^i, \hat{s}\big) d\Omega}, \quad (6)$$

where $\hat{s}_0^i$ are the centers of the N footprints used for the interpolation. In our BG implementation, $N = 6$ was selected based on a tradeoff between accuracy and latency.

A detailed description of the Backus-Gilbert interpolation implementation for SMAP can be found in [10] and the assessment of the enhanced product can be found in [11].

To correct the land and water TBs the SMAP measurements were separated into two sets according to the location of the center of the antenna footprint: one for centers located over land and the other with centers located over water. We first correct the TB over the set of centers located over land and then we correct the TB over the set of centers located over water.

A. Correction of Data with Centers over Land

From (3) replacing T_B^{water} by an estimate $\hat{T}_B^{water}$, T_B^{land} can be obtained as:

$$T_B^{land} = \frac{T_B - f \hat{T}_B^{water}}{1 - f} \quad (7)$$

To estimate the TB over water, $\hat{T}_B^{water}$, we search for measurements with the footprint center located over water and with a water fraction greater than a pre-fixed threshold to assure the selection of near-contamination-free measurements. The

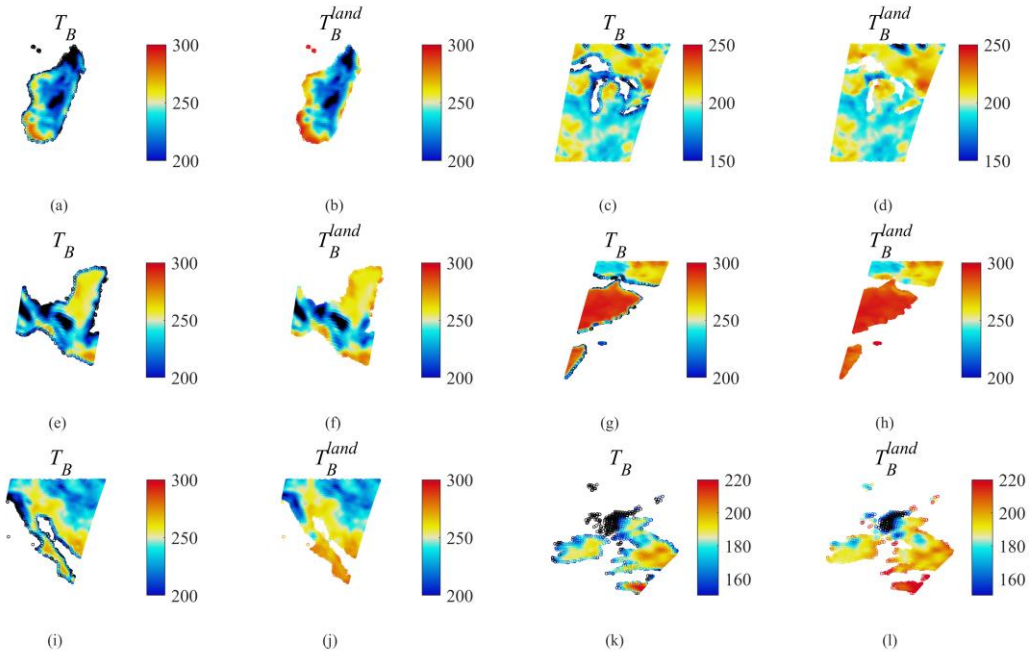

Fig. 2. Results obtained using simulated data. Column 1 and 3: The SMAP simulated measurements before correction. Columns 2 and 4: Corrected land TB. The simulated regions are: (a) and (b) Madagascar, (c) and (d) Great Lakes, (e) and (f) Yucatan Peninsula, (g) and (h) Arabian Sea, (i) and (j) Baja California and (k) and (l) United Kingdom.

extent of the searching region is also pre-fixed to assure that we can find measurements that satisfy the threshold condition. If measurements satisfying the threshold condition are not found within the region, then a default value is used. The default value is the average of all the measurements on the SMAP half-orbit pass satisfying the threshold condition and not contaminated by sea ice. In Section III, the selection of these pre-fixed parameters of water fraction and searching extent is determined through simulations.

B. Corrections of Data with Centers over Water

From (3) replacing T_B^{land} by an estimate $\hat{T}_B^{land}$, T_B^{water} can be obtained as:

$$T_B^{water} = \frac{T_B - (1-f)\hat{T}_B^{land}}{f} \tag{8}$$

The estimation of the land surface TB following a similar algorithm, as in Section II.*A*, is challenging due to the greater variance of the land TBs which is a significant source of errors for the correction algorithm. In addition, searching for measurements free of contamination requires looking into regions away from the coastal zones leading to averaged TBs that might not be representative of the actual coastal TB.

Therefore, an alternative method was adopted by modifying the algorithm to mitigate those challenges. Taking advantage of the already corrected land temperatures, as in Section II.*A*, we can reduce the search area and allow for the selection of corrected land TBs closer to the coastal zone without imposing water fraction conditions (these measurements are much less affected by contamination). Then, the inverse distance weighted average temperature was obtained from radiometer measurements already free of contamination.

The approach to estimate $\hat{T}_B^{water}$ and $\hat{T}_B^{land}$ is data-driven using SMAP data itself. It has the advantage of computational efficiency and does not require external ancillary data.

III. Simulated Data and Retrieval Results

The lack of in situ data over areas affected by water contamination limits the ability to validate the correction algorithm. To mitigate this problem simulated data was used to evaluate the performance and to study the sensitivity of the algorithm to different parameters, mainly the water fraction threshold and the extent of the search areas to estimate the land and water TB mentioned in the previous section.

The SMAP brightness temperature T_B were simulated as shown in (1), ignoring atmospheric and galactic effects. In the integrand of (1) the brightness temperature T_b over land surface is computed using a smooth surface model taking into account the physical surface temperature, the frequency (1.414 GHz), the incidence angle (~40 degrees) and the dielectric constant which is computed using the Mironov's model [12]. The model for the T_b over water follows the method presented in [13], which takes into account wind, sea surface temperature, and salinity. The clay fraction, needed to compute the dielectric constant, was obtained from the Harmonize world soil database (HWSD), the land surface soil moisture and temperature were provided by the Global Modeling Assimilation Office (GMAO) (https://gmao.gsfc.nasa.gov/) land surface models, while the wind, water temperature and salinity were provided by the

National Center for Environmental Prediction Global Data Assimilation System (GDAS) (https://www.ncdc.noaa.gov/data-access/model-data/model-datasets/global-data-assimilation-system-gdas).

To evaluate the performance of the algorithm, the uncorrected and corrected TB were compared against to what we consider to be the true TB, the integrated T_b over the antenna 3dB beam from land only

$$T_{B_{land}}^{3dB}(\hat{s}_0) = \frac{\int G(\hat{s}_0,\hat{s})(1-M(\hat{s}))T_b(\hat{s})d\Omega_{3dB}}{\int G(\hat{s}_0,\hat{s})d\Omega_{3dB}}, \qquad (9)$$

where Ω_{3dB} is the 3dB beam domain of integration.

The T_B and $T_{B_{land}}^{3dB}$ were simulated for six different regions and then the corrected T_B^{land} was computed as it was stated in Section II.*A*, see Fig. 2. The uncorrected T_B and the corrected T_B^{land} were compared against $T_{B_{land}}^{3dB}$. The tested regions were selected to cover different types of coastlines and water bodies. Before applying the algorithm, two parameters (water fraction threshold and the dimensions of the searching area) need to be set in order to estimate $\hat{T}_B^{water}$. Fig. 3 displays the mean, standard deviation (STD) and the root mean square (RMS) of the differences ($T_B - T_{B_{land}}^{3dB}$), as a function of distance to water bodies (top row) and as a function of water fraction (bottom row) for different threshold values. To evaluate the statistics as a function of distance to water bodies, the data were binned into 2 km bins and then the mean, STD and RMS of differences were evaluated for each bin. To evaluate the statistics as a function of water fraction the data were binned into 0.1 water fraction increments. Those results show that the performance improves when the threshold gets closer to one (red line). We also observe that the performance significantly deteriorates as the water fraction tends to one (footprint on small pieces of land surrounded by water). Indeed, the plots as a function of distance to the water body (top row) show that before correction was applied the mean difference at 0 km from the water body was ~33.0 K and after correction, this difference was reduced to approximately -3.5 K, -2.0 K and -0.7 K for thresholds 0.8, 0.9 and 0.99 respectively. We also see that, while the uncorrected differences reach the -1.0 K mean value at ~12 km distance from the coast, the corrected differences reach the same level at 2.5 km, 1.5 km and 0 km for thresholds 0.8, 0.9 and 0.99 respectively. Note that all the lines merge after 20 km reaching a level of about 1.0 K. This shows the limitation of the algorithm to correct beyond that level due to limitations in the beam pattern's correction algorithm. The STD and RMS plots show that the uncertainties were also reduced significantly after correction. The figure shows that at 0 km from the closest coast the STD and RMS were ~32.0 K and ~45.0 K, respectively and those values were reduced to ~8 K, ~6 K and ~4 K for thresholds 0.8, 0.9 and 0.99, respectively and reaching 3.5 K 2 km away from the water bodies. All the lines merge 15 km away from the coast. Fig. 3 bottom row shows that the mean value of ($T_B - T_{B_{land}}^{3dB}$) decreases rapidly before corrections reaching -50 K at f=0.4 while after correction the mean values are ~-3 K, -2 K and -1 K at the same water fraction value. We also observe that for threshold = 0.99 the mean value never gets smaller than -10 K and stays within the -3K range at about f = 0.68. The STD and RMS plots as a function of water fraction also show that for threshold = 0.99 the STD and RMS stay below 5.0 K for f < 0.6. Fig. 4 displays the statistics from results obtained for different search area dimensions showing that the size of the area does not affect the incoming results. Thus, based on the sensitivity

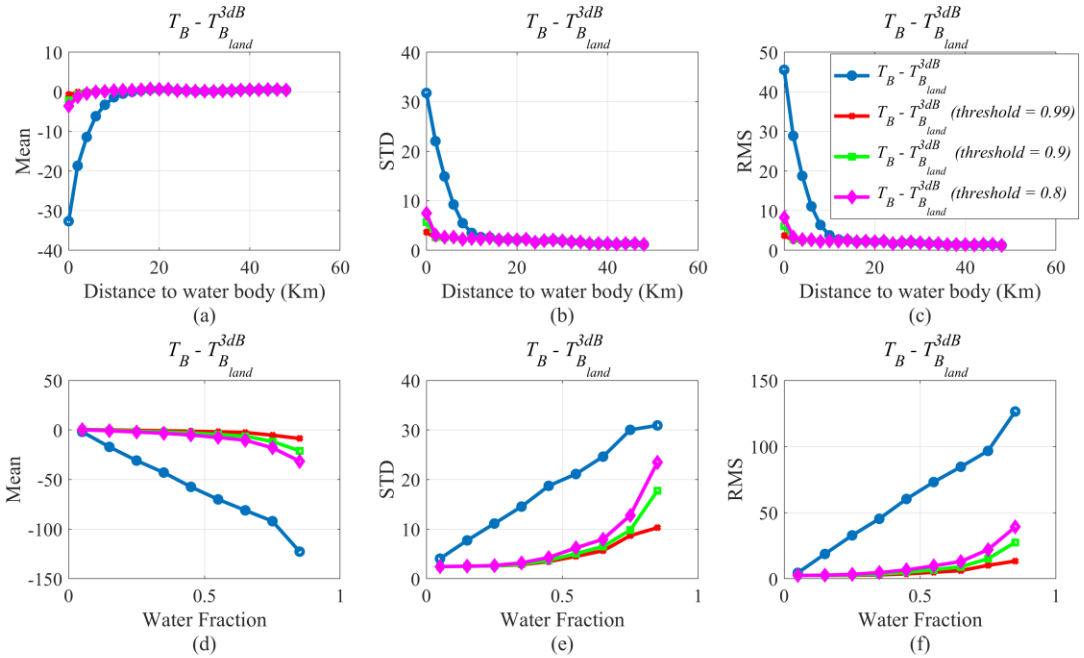

Fig. 3. Mean, STD, and RMSE resulting from the water contamination correction. We display the difference of uncorrected T_B - $T_{B_{land}}^{3dB}$ (blue line) and corrected T_B -$T_{B_{land}}^{3dB}$ for several thresholds (0.99, 0.9, 0.8). Top row displays statistics as a function of distance to water bodies. Bottom row displays statistics as a function of water fraction.

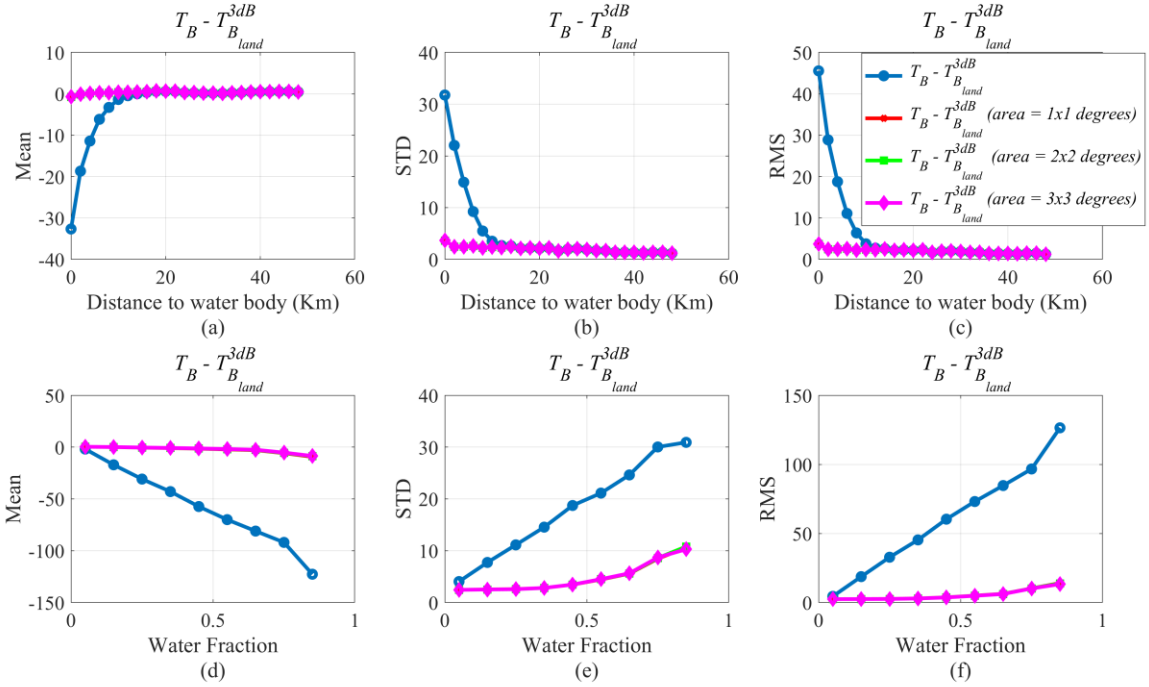

Fig. 4. Mean, STD, and RMSE resulting from the water contamination correction. We display the difference of uncorrected T_B - $T_{B_{land}}^{3dB}$ (blue line) and corrected T_B -$T_{B_{land}}^{3dB}$ for several searching areas (1x1 degrees, 2x2 degrees and 3x3 degrees). Top row displays statistics as a function of distance to water bodies. Bottom row displays statistics as a function of water fraction.

results we set the water fraction threshold to 0.99 and the search area dimension to 3x3 degrees latitude/longitude to ensure that we have enough measurements within the area under consideration to satisfy the threshold condition. Fig. 2 displays maps of the uncorrected land T_B (columns 1 and 3) and the corrected T_B^{land} (columns 2 and 4) for six regions including islands, lakes and challenging coastal lines. We have (a) and (b) Madagascar, (c) and (d) Great Lakes, (e) and (f) Yucatan Peninsula, (g) and (h) Arabian Sea, (i) and (j) Baja California and (k) and (l) United Kingdom. We noticed that the smooth transition between land and water was eliminated after correction creating sharper edges at the coastal lines. Other noticeable features: 1) the islands present in Fig. 2 (a) Comoros and Mayotte, (g) Socotra Island, (i) Isla Guadalupe and (k) Faroe Island, characterized by very low temperatures (color blue) before correction, were significantly corrected reaching temperature levels comparable to the range of inland temperatures, 2) in Fig. 2 (c) it is clear how the low temperatures (blue rings) surrounding the lakes were eliminated after correction, 3) Fig. 2 (i) shows the elimination of the contamination caused by the Salton Sea located at approximately 33° N and 116°W.

We then correct T_B^{water} as stated in Section II.*B* of the previous section and we compare it against the corresponding 3 dB TB contribution from water given by

$$T_{B_{water}}^{3dB}(\hat{s}_0) = \frac{\int G(\hat{s}_0,\hat{s})M(\hat{s})T_b(\hat{s})d\Omega_{3dB}}{\int G(\hat{s}_0,\hat{s})d\Omega_{3dB}}. \qquad (8)$$

To estimate $\hat{T}_B^{land}$ we need to set the dimension of the search area. Fig. 5 displays the statistical results for corrected water TB comparing different cases: area dimension 1x1 degrees, 2x2 degrees, and 3x3 degrees and water fraction threshold set to 0.99. Results for the suggested alternative method as explained in Section II.*B* were added setting the searching area to 1x1 and allowing the selection of already corrected temperatures. The figure shows that the performances are very similar for the first three cases and the solution improves significantly when the alternative method is used (black line). The absolute mean value was reduced to less than 2 K for all water fractions when the alternative method is applied. We also see that for small values of water fraction (small lakes) the uncertainty of the water TB is high, reaching ~ 20 K for f = 0.2 but for f =0.5 the levels of uncertainty were reduced to about 5 K. In light of those results, the searching area for the estimation of $\hat{T}_B^{land}$ was set to 1x1 degrees latitude/longitude and the alternative method was adopted. Maps of uncorrected water T_B and corrected T_B^{water} are displayed in Fig. 6. We see how the dark edges on the left column maps disappear after correction. We also observed that some hot spots in the water caused by the presence of islands disappeared after correction, for example in the figures for Madagascar, Arabian Peninsula and Baja California.

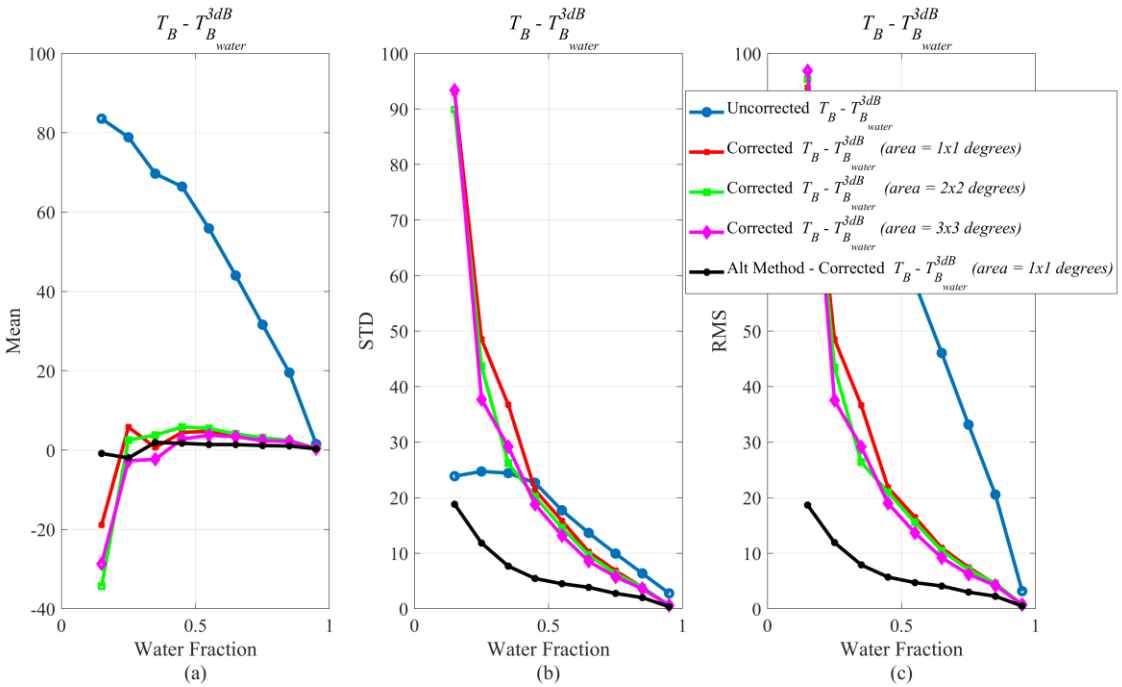

Fig. 5. Statistics. Mean , STD, and RMS resulting from the land contamination correction as a function of water fraction. We display the difference of uncorrected $T_B - T_{B_{water}}^{3dB}$ (blue line) and corrected $T_B - T_{B_{water}}^{3dB}$ for several searching areas (1x1 degrees (red line), 2x2 degrees (green line) and 3x3 degrees (magenta line)). We also incorporate the results obtained using the alternative method (black line).

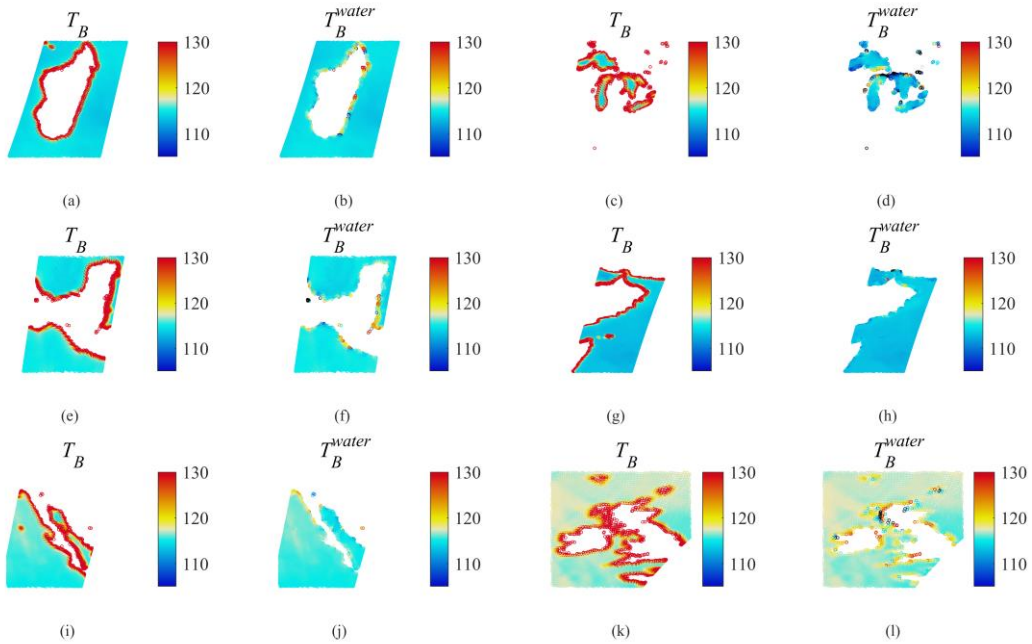

Fig. 6. Results obtained using simulated data. Column 1 and 3: The SMAP simulated measurements before correction. Columns 2 and 4: Corrected water TB. From top to bottom, we (a) and (b) Madagascar, (c) and (d) Great Lakes, (e) and (f) Yucatan Peninsula, (g) and (h) Arabian Sea, (i) and (j) Baja California and (k) and (l) United Kingdom.

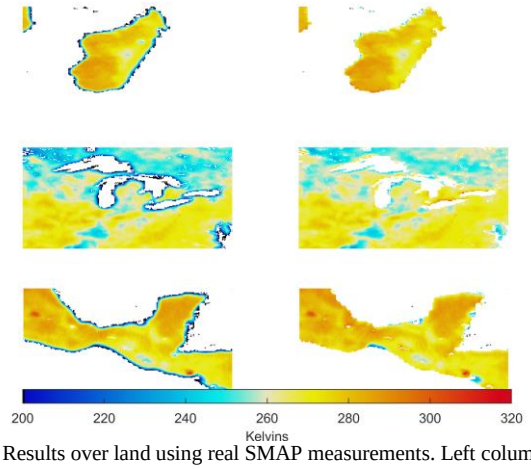

Fig. 7. Results over land using real SMAP measurements. Left column: uncorrected data. Right column: corrected land TB.

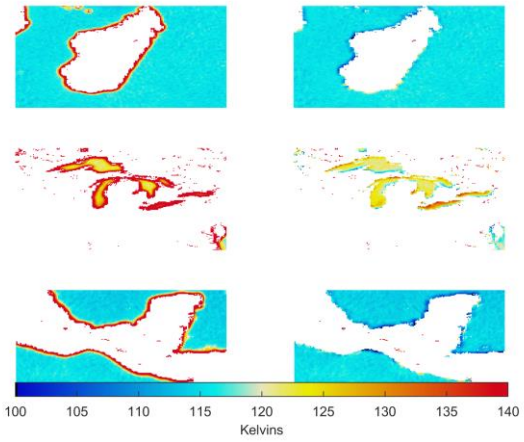

Fig. 8. Results over land using real SMAP measurements. Left column: uncorrected data. Right column: corrected water TB.

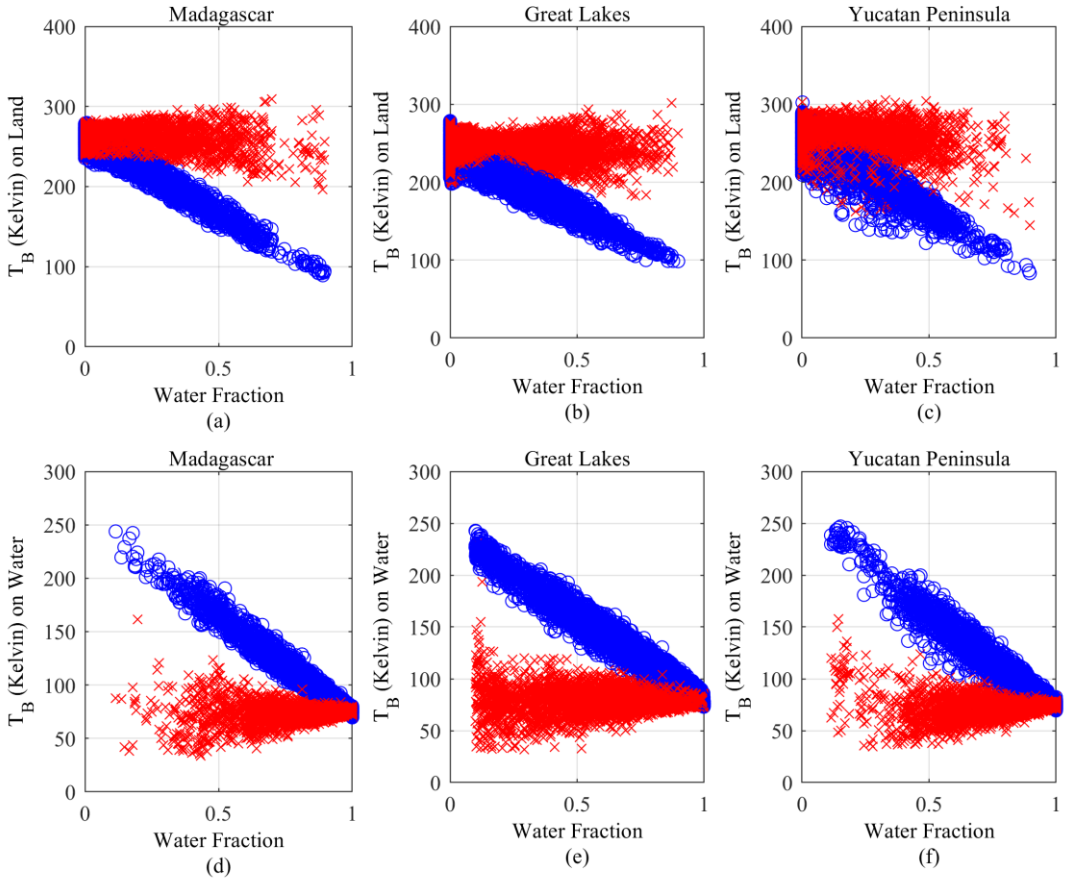

Fig. 9. Scattering plot of uncorrected T_B (blue circles) and corrected T_B (red times) as a function of water fraction. Top row, T_B H polarization on land. Bottom row, T_B H polarization on water. Left column: Madagascar, center column: Great Lakes and right column: Yucatan Peninsula. Before correction the T_B decreases with water fraction and after correction, we removed that dependence.

IV. Application to SMAP data

The results over real data were obtained following the same algorithm described in the previous section. We should not expect the same results obtained with simulated data due to the presence of other sources of errors when dealing with real data such as geolocation errors, greater variability of TB (vegetation, urban areas…), etc. Fig. 7 and Fig. 8 display local images of

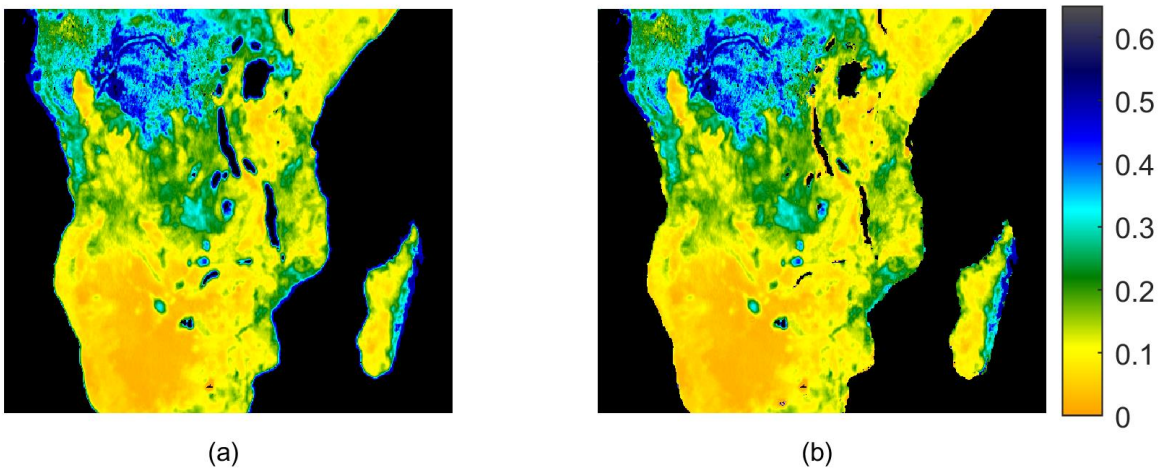

Fig. 10. Retrieved Soil Moisture map of Central Africa and Madagascar. (a) Uncorrected soil moisture. (b) Corrected soil moisture. Data corresponds to July 1-3, 2017. The correction clears the wet areas around Lake Victoria and other lakes in the area. The cyan band on the east coast of Africa was removed. The Madagascar Island shows sharper edges after correction, the cyan band on the coast of the island was eliminated

aft-look T_B for the V polarization for June 1-3/2018 obtained from the SMAP L1C enhanced product. Fig. 7 displays uncorrected land T_B on the left and corrected land T_B on the right. We observe that the intense blue borders corresponding

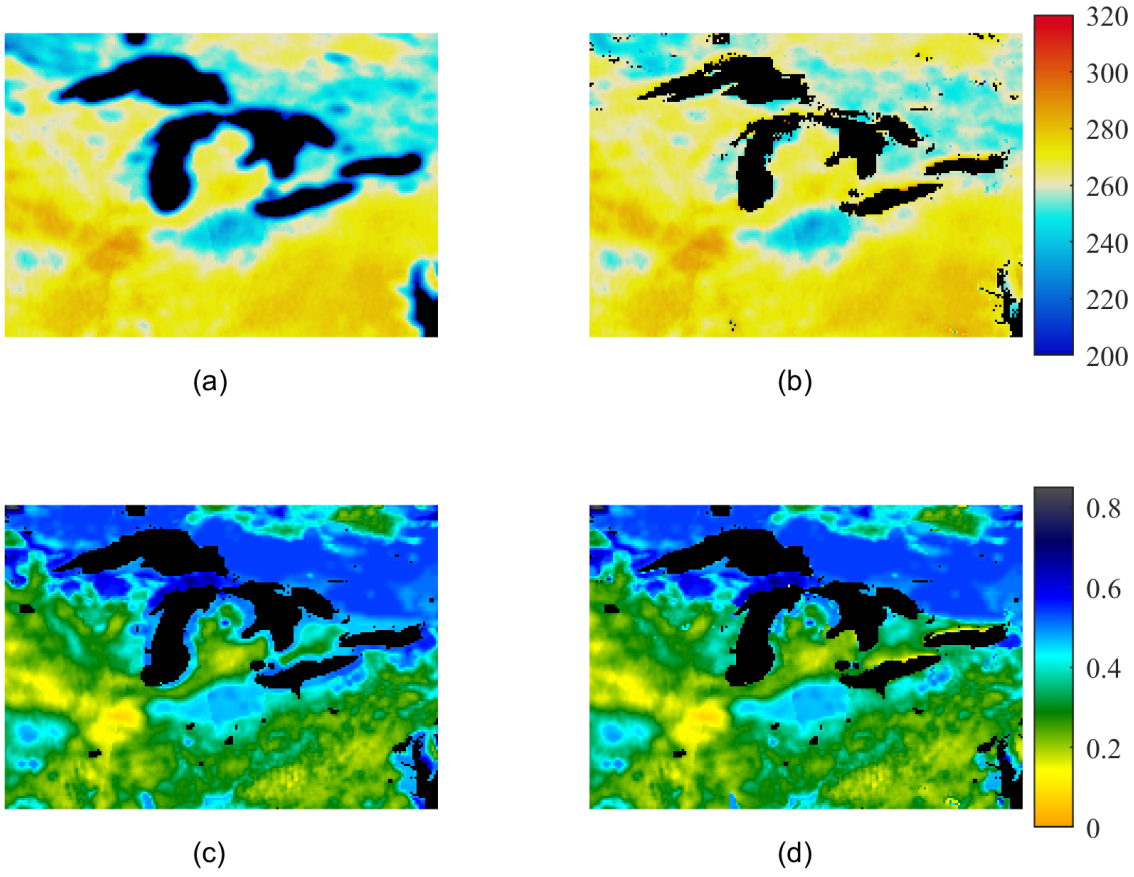

Fig. 11. Great Lakes. (a) Uncorrected TB and (b) corrected TB. (c) and (d) Corresponding retrieved soil moisture. Data corresponds to July 1-3 2017. The effect of water correction on the TB level is illustrated by sharper edges around the lakes.

TABLE I. MEAN VALUES OF DIFFERENCES FOR DIFFERENT METRICS. WE EVALUATED CORRECTED SM M – UNCORRECTED SM M WHERE M REPRESENTS THE METRICS RMSE, UBRMSE, BIAS, MABIAS AND R. N IS THE NUMBER OF STATIONS.

water frac %	Δ RMSD		Δ ubRMSD		Δ bias		Δ MABias		Δ R		N
	AM	**PM**	**AM**	**PM**	**AM**	**PM**	**AM**	**PM**	**AM**	**PM**	
0 - 5	-0.003	-0.003	0	0	-0.006	-0.006	-0.003	-0.004	0.007	0.007	401
5-10	-0.021	-0.021	-0.002	-0.002	-0.03	-0.029	-0.021	-0.021	0.022	0.028	37
10-15	-0.013	-0.012	0	0	-0.013	-0.012	-0.013	-0.012	0.003	0.004	9
15-20	-0.072	-0.068	-0.008	-0.005	-0.1	-0.103	-0.073	-0.07	0.127	0.082	5
20-25	-0.03	-0.029	0	-0.001	-0.032	-0.032	-0.031	-0.031	-0.011	0.005	4
25-30	-0.04	-0.038	0.006	0.006	-0.044	-0.041	-0.042	-0.039	0.107	0.1	7
30-35	-0.068	-0.052	0.011	0.015	-0.077	-0.061	-0.076	-0.06	0.217	0.217	2
35-40	0	0	0	0	0	0	0	0	0.042	0	3
40-45	-0.098	-0.102	0.041	0.012	-0.112	-0.106	-0.112	-0.106	0.103	0.125	2
45-50	-0.177	-0.162	0.03	0.029	-0.204	-0.181	-0.193	-0.178	0.38	0.45	2

to cold temperatures in the coastal areas were removed after correction. Fig. 8 shows the uncorrected (left column) and corrected (right column) water T_B. The elimination of warm temperatures near the coastal areas is significant but some anomalies are observed. We see in some areas that the corrected T_B over water bodies are underestimated, for example over the west coast of Madagascar (Fig. 8 (top right)) or over both coasts of the Yucatan Peninsula (Fig. 8 (bottom right)). We suspect that residual pointing errors may be the cause of those errors. Fig. 9 displays scatter plots of T_B as a function of water fraction before (in blue) and after (in red) correction for different regions. On the top row, we show the temperatures over land and on the bottom row we show the temperatures over water. After correction, we observed that all dependence on water fraction was essentially eliminated. We also observed increasingly scattered data, in particular at high water fraction for Fig. 9 top row (small islands) and low water fraction for Fig. 9 bottom row (small lakes). Detailed information about the data used in this section is found in [14]-[16].

Fig. 10 (a) displays the retrieved soil moisture before correction and (b) after correction in Central Africa and the Madagascar Island. It is noticeable how the correction clears the wet areas around Lake Victoria and other lakes in the area. The cyan band on the east coast of Africa were removed. The Madagascar Island shows sharper edges after correction, the cyan band on the coast of the island were eliminated. Fig. 11 (a) and (b) displays uncorrected and corrected TB maps of the Great Lake and Fig. 11 (c) and (d) the corresponding retrieved soil moisture. The effect of water correction on the TB level is illustrated by sharper edges around the lakes.

V. VALIDATION OVER SPARSE NETWORK STATIONS

The baseline SMAP validation for the soil moisture product is a comparison of retrievals with ground-based observations that have been verified as providing a spatial average of soil moisture at the same scale, referred to as core validation sites (CVS) in the SMAP Calibration / Validation Plan. Those CVS were selected to avoid water contamination in our satellite measurements over those areas, thus making them inadequate for validating the water correction algorithm performance. The data from CVS is supplemented by other sources of observations to include a wider range of conditions such as data from sparse networks. Examples of sparse networks include the United States Department of Agriculture (USDA) Soil Climate Analysis Network, the NOAA Climate Research Network and the Oklahoma Mesonet.

To validate the algorithm the data from the SMAP L1C_E enhanced product was compared with the data available from all the stations on the sparse network. For each station we evaluate the RMSD, bias, unbiased RMSD (ubRMSD), mean absolute bias (MABias) and correlation coefficient (R) for the corrected and uncorrected Soil Moisture (SM) and then the differences between those metrics (corrected - uncorrected) were evaluated. The stations were then grouped according to their water fraction content (5% intervals) and the mean values of the differences were then computed. Table I shows the mean values of the metric differences for each water fraction bin level (column 1). Column 2 corresponds with the mean value of corrected SM RMSD – uncorrected SM RMSD for AM data; the negative values indicate the improvement of this metric after correction for all water fraction levels. Columns 4, 6 and 8 correspond with the mean value of differences in ubRMSD, bias and MAbias respectively for AM data; negative values indicate an improvement for all levels of water fraction (below 25% in the MAbias case). Column 10 displays corrected SM R – uncorrected SM R; in this case positive values indicate an improvement in correlation after correction. Columns 3, 5, 7, 11 display similar metrics for PM data and show the same performance as the AM data. Table I shows that the majority of stations (401) have water fraction content less than 5% and that for that level, while there is no improvement in the ubRMSD, there is a reduction in RMSD, bias and MAbias and an increase in correlation. For water fraction levels between (5% and 10%) the number of stations is 37 and we can observe an improvement in ubRMSD of ~5% if we consider the 0.04% requirement.

VI. CONCLUSIONS

The SPA algorithm together with a data-driven approach for land and water TB estimation was implemented to improve the TB measurements over coastal areas and near bodies of water. Results over simulated data show significant statistical improvements. Results over real data show that the presented algorithm minimizes the cold borders over land and the warmer borders over ocean. The dependence on water fraction was minimized after correction. The validation over the sparse network stations shows a better performance on SM after T_B

over land was corrected. The benefits seen in the soil moisture retrievals were significant. The implementation of the SPA adds ~10 to 15 minutes to the run time to process one revolution of the TB product (Level 1B), and is feasible for operational and near real time processing. We concluded that the SPA is an effective and computationally efficient algorithm for improving SMAP TB and Soil Moisture retrievals near water bodies.

ACKNOWLEDGMENT

This work is carried out by the Jet Propulsion Laboratory, California Institute of Technology, under a contract with the National Aeronautics and Space Administration.

REFERENCES

[1] D. Entekhabi et al. “The Soil Moisture Active Passive (SMAP) Mission”, *Proceedings of the IEEE*, vol. 98, no. 5, pp. 704-716, May 2010. DOI: 10.1109/JPROC.2010.2043918

[2] R. Bennartz, “On the use of SSM/I measurements in coastal regions”, *J. Atmos. Ocean. Technol.*, vol. 16, no. 4, pp. 417–431, Apr. 1999.

[3] N. Maaß, L. Kaleschke, “Improving passive microwave sea ice concentration algorithms for coastal areas: Applications to the Baltic Sea”, *Tellus*, vol. 62A, pp. 393–410, 2010. DOI:10.1111/j.1600-0870.2010.00452.x.

[4] T. Bellerby, M. Taberner, A. Wilmshurst, M. Beaumont, E. Barrett, C. Durbin, and J. Scott, “Retrieval of Land and Sea Brightness Temperatures from Mixed Coastal Pixels in Passive Microwave Data,” *IEEE Trans. Geosci. Remote Sensing*, vol. 36, pp. 1844–1851, Nov. 1998.

[5] J. X. Yang, JD. S. Mckague, C. S. Ruf, “Land contamination correction for passive microwave radiometer data: Demonstration of wind retrieval in the Great Lakes using SSM/I”. *J. Atmos. Ocean. Technol*, vol 31, pp. 2094–2113, Oct. 2014.

[6] C. Desportes, E. Obligis, L. Eymard, “On the wet tropospheric correction for altimetry in coastal regions,” *IEEE Trans. Geosci. Remote Sens.*, vol. 45, no. 7, pp. 2139–2149, Jul. 2007. DOI: 10.1109/TGRS.2006.888967

[7] J. Chaubell, S. Yueh, J. Peng, S. Chan, S. Dunbar, D. Entekhabi, "Improving Brightness Temperature Measurements Near Coastal Areas", *Geoscience and Remote Sensing Symposium IGARSS 2018 - 2018 IEEE International*, pp. 3758-3761, 2018.

[8] G. Backus and F. Gilbert, “Uniqueness in the inversion of inaccurate gross earth data,” Phil. Trans. R. Soc. London, vol. A266, Mar 1970.

[9] G. Poe, “Optimum Interpolation of Imaging Microwave Radiometer Data”, *IEEE Transactions on geoscience and remote sensing*, vol. 28. no. 5, pp. 800-810. Sept. 1990

.[10] J. Chaubell, “SMAP Algorithm Theoretical Basis Document: Enhanced L1B Radiometer Brightness Temperature Product**”** Jet Propulsion Laboratory, California Institute of Technology, Pasadena, CA, 2016. (JPL D-56287) https://nsidc.org/sites/nsidc.org/files/technical-references/SMAP_L1B_TB_E_Product_ATBD_D-56287.pdf

[11] S. K. Chan, R. Bindlish, P. O'Neill, T. Jackson, E. Njoku, S. Dunbar, et al. “Development and assessment of the SMAP enhanced passive soil moisture product.” *Remote Sensing of Environment*, vol. 204, pp. 931– 941, Jan. 2018. DOI: 10.1016/j.rse.2017.08.025

[12] V. L. Mironov, L. G. Kosolapova, S. V. Fomin, ”Soil dielectric model accounting for contribution of bound water spectra through clay content", *PIERS Online*, vol. 4, no. 1, pp. 31-35, July 2008. DOI: 10.1109/TGRS.2008.2011631

[13] S. Yueh and J. Chaubell, “Sea surface salinity and wind retrieval using combined passive and active L-band microwave observations,” *IEEE Trans. Geosci. Remote Sens.*, vol. 50, no. 4, pp. 1022–1032, Apr. 2012.

[14] M. J. Chaubell, S. Chan, R. S. Dunbar, J. Peng, and S. Yueh, “SMAP Enhanced L1C Radiometer Half-Orbit 9 km EASE-Grid Brightness Temperatures”, Version 1, 2016. Boulder, Colorado USA. NASA National Snow and Ice Data Center Distributed Active Archive Center. DOI: 10.5067/2C9O9KT6JAWS.

[15] S. Chan, E. Njoku, A. Colliander, “SMAP L1C Radiometer Half-Orbit 36 km EASE-Grid Brightness Temperatures. Version 3”. Boulder, Colorado USA: NASA National Snow and Ice Data Center Distributed Active Archive Center, 2016. DOI:10.5067/E51BSP6V3KP7.

[16] J. R. Piepmeier, P. N. Mohammed, J. Peng, E. Kim, G. De Amici, and C. Ruf. “SMAP L1B Radiometer Half-Orbit Time-Ordered Brightness Temperatures”. Version 3, Boulder, Colorado USA: NASA National Snow and Ice Data Center Distributed Active Archive Center, 2016. DOI: YV5VOWY5V446.